Preparation and electrochemical properties of mesoporous Carbon@ MoS2 anode materials for lithium-ion batteries

International Journal of Electrochemical Science 21 (2026) 101294

Contents lists available at ScienceDirect

International Journal of Electrochemical Science

journal homepage: www.sciencedirect.com/journal/international-journal-of-electrochemical-science

Preparation and electrochemical properties of mesoporous Carbon@ MoS_2 anode materials for lithium-ion batteries

Jiazhe Sun [a], Zhao Xu [a], Wenyu Wang [b], Shuqi Sheng [b], Shengyi Zhao [b], Yifei Chen [b], Huhao Kong [b], Yuqi Liu [b], Xiaoping Jiang [c], Yongchao Yao [d], He Chen [d], Jia Wei Chew [e], Zhengping Zhao [b,*]

[a] College of Materials Science and Engineering, Zhejiang University of Technology, Hangzhou 310014, China
[b] Zhijiang College, Zhejiang University of Technology, Shaoxing 312000, China
[c] Transfar Zhilian Co., Ltd., Hangzhou 310014, China
[d] Zibo Qixiang Tengda Chemical Co., Ltd., Zibo 255400, China
[e] Chemical Engineering, Chalmers University of Technology, Gothenburg 41296, Sweden

ARTICLE INFO

Keywords:
MoS_2
Lignin
Lithium-ion batteries
Porous structure
Anode material

ABSTRACT

Addressing the escalating demand for high-performance lithium-ion batteries (LIBs) in light of the energy crisis and environmental concerns, this study aimed to develop an advanced anode material. To overcome the limitations of conventional graphite anodes, a novel NG@MoS_2@LS-C composite was synthesized via a hydrothermal method combined with lignin–carbon coating and carbonization. Specifically, MoS_2 nanoparticles were uniformly deposited on the surface of natural graphite, followed by lignin–carbon coating and carbonization, resulting in a unique structure with enhanced electrochemical properties. The experimental results show that the incorporation of MoS_2 nanoparticles significantly improved cycling performance, while the lignin–carbon coating mitigated volume expansion, enhancing cycle stability. The composite exhibited an initial capacity of 588.2 $mAh{\cdot}g^{-1}$ and retained a reversible capacity of 326.2 $mAh{\cdot}g^{-1}$ after 30 cycles, outperforming pristine graphite. In addition, the lamellar structure of MoS_2 nanoparticles, combined with the buffering and electrolyte blocking effects of a lignin-derived carbon shell, endows the composite with low charge transfer resistance and a high lithium-ion diffusion rate, resulting in excellent electron-ion cooperative transmission characteristics. This study presents a promising anode material for next-generation LIBs, which can contribute towards green and sustainable energy storage solutions.

1. Introduction

As the global population grows, the demand for energy continues to soar, exacerbating the energy crisis and environmental pollution stemming from the utilization of traditional fossil fuels (namely, coal, oil, and natural gas). The inherent non-renewability of these fuels underscores their unsustainable nature, necessitating the urgent development and advancement of green, clean, and renewable energy sources [1]. Lithium-ion batteries (LIBs), well acknowledged for their high energy density and extended lifespan, have emerged as a pivotal energy storage device. Since their commercialization by Sony Corporation in the 1990s, LIBs have been widely adopted in electronic devices, medical instruments, electric vehicles, aerospace applications, and beyond [2]. However, the escalating demands for electrical devices with higher current, higher power, and longer endurance have increasingly exceeded the capabilities of existing LIBs in terms of energy density, power density, and cycle life. Consequently, the development of anode materials with high specific capacity, superior cycle efficiency, enhanced safety performance, and low cost has become a key research focus to elevate LIB performance and stimulate the evolution of next-generation LIBs [3].

Graphite, abundant in nature and lauded for its excellent cycle stability and low operating potential, has long served as the primary anode material in commercial LIBs. However, its limited specific capacity and poor rate charge-discharge capability render it inadequate for the requirements of next-generation LIBs. To address these limitations, researchers have explored various chemical modification strategies, including element doping, oxidation treatment, and surface loading, to

* Corresponding author.
E-mail addresses: sunjiazhe121@163.com (J. Sun), zhengping_zhao@126.com (Z. Zhao).

https://doi.org/10.1016/j.ijoes.2026.101294
Received 25 November 2025; Received in revised form 12 January 2026; Accepted 12 January 2026
Available online 13 January 2026

enhance the electrochemical properties of graphite [4].

Layered inorganic materials such as MoS_2 and WS_2 have garnered significant interest [5]. These prototypical layered transition metal sulfides, featuring a graphite-like structure conducive to the intercalation and deintercalation of Li^+ , represent promising candidates for next-generation LIB anode materials. MoS_2, specifically, adopts a layered stacking configuration with Mo atoms sandwiched between two layers of S atoms. The weak van der Waals forces and large interlayer spacing facilitate rapid Li^+ diffusion. Unfortunately, the volumetric expansion of MoS_2 nanoparticles during cycling leads to reduced capacity, impeding its widespread adoption as an LIB electrode material [6–8].

Lignin, an amorphous biomass-based polymer that is the second most abundant in nature (with cellulose being the most abundant) [9–11], boasts high carbon content and high calorific value, which makes it an ideal carbon source for constructing hierarchical porous structures. The multi-level pore architecture, high specific surface area, and excellent electrical conductivity render it promising for modifying graphite to improve its electrochemical performance. However, lignin remains underutilized in industrial production. Harnessing lignin to develop carbon-based composites integrated with transition metal oxides or sulfides as LIB anode materials not only enhances the electrochemical performance of LIBs, but also allows for exploitation of a renewable resource and thus aligns with the principles of green and sustainable development [12].

Herein, we report a novel modification strategy for natural graphite, utilizing MoS_2 and sodium lignosulfonate. By employing a hydrothermal method, MoS_2 nanoparticles were uniformly deposited on the surface of natural graphite, followed by lignin–carbon coating and carbonization to yield a lignin–carbon-coated MoS_2 nanoparticle-loaded natural graphite-based LIB anode material (NG@MoS_2@LS-C). In contrast to prior studies, the present work adopts a one-step hydrothermal approach for MoS_2 loading, which is characterized by a more streamlined experimental protocol and tunable MoS_2 loading capacities. [13]. Therefore, this method exhibits higher operability and cost-effectiveness. The integration of MoS_2 nanoparticles boosts the cyclic performance of the composite, while the lignin-derived carbon coating layer alleviates volume expansion during cycling, consequently enhancing the material's cycling stability [14]. Experimental results indicate that this composite material holds promise for application in the field of LIB anode materials.

2. Experimental

2.1. Chemicals

Graphite powder particles were obtained through crushing and ball milling of commercially purchased graphite ore (natural flake graphite), which was purchased from Sinoma International Engineering Co., Ltd (Jiangsu, China). Sodium molybdate (Na_2MoO_4, 99 %), thiourea (CH_4N_2S, AR, 99 %), and n-butanol (C_4H_9OH, AR, 99 %) were procured from Sinopharm Chemical Reagent Co., Ltd (Shanghai, China). Sodium lignosulfonate ($C_{20}H_{24}NaO_{10}S_2$, molecular weight uncertainty) and N-methylpyrrolidone (NMP, AR, 99 %) were sourced from Aladdin Reagent (Shanghai, China). Battery separators, lithium foils, copper foils, acetylene black, binder (PVDF), and electrolyte were purchased from Hefei Kejing Materials Tech Co., Ltd (Hefei, China). High-purity argon gas (99.99 %) was obtained from Hangzhou Bestgas Co., Ltd (Hangzhou, China).

2.2. Preparation of NG@MoS_2

Firstly, the natural graphite ore was crushed for 1 min by a crusher, and then the crushed graphite was ball-milled for 10 min by a planetary ball mill to obtain graphite powder with appropriate particle size. A targeted amount of natural graphite powder was dispersed in deionized water. Subsequently, solid powders of sodium molybdate and thiourea with a molar ratio of 1:1 were added to the graphite dispersion. The mixture was homogenized using a constant temperature magnetic stirrer for 10 min and then transferred to a hydrothermal reactor for a 10-h reaction at 180 °C. After the reaction, the product was centrifuged at 3000 rpm for 10 min and washed three times with water to obtain NG@MoS_2.

2.3. Preparation of NG@MoS2@LS-C

A measured quantity of the prepared NG@MoS_2 composite was dispersed in an aqueous solution containing sodium lignosulfonate (NG@MoS_2:LS = 1:5), followed by stirring until a uniform dispersion was achieved. This dispersion was then added dropwise to 400 mL of n-butanol under mechanical stirring. The resultant mixture was filtered, transferred to a vacuum oven, and dried at 60 °C for 24 h to obtain the pre-carbonized NG@MoS_2@LS. The dried composite was placed in a ceramic boat and calcined in a tube furnace under an argon atmosphere at 800 °C for 2 h to yield NG@MoS_2@LS-C.

2.4. Sample characterization

The surface morphology of the samples was characterized using scanning electron microscopy (Oberkochen, German, ZEISS Sigma 300, EHT=3.00 kV). Elemental analysis was performed using an energy-dispersive spectrometer (Oberkochen, German, NPONTS: 2048, BEAMKV: 15 kV, CHOFFSET: 20). Nitrogen adsorption-desorption tests were conducted on the samples using a surface area and pore size analyzer (GA, USA, Micromeritics ASAP 2460) to evaluate their specific surface area and pore size distribution. Firstly, the sample was degassed at 120 °C for 8 h, and then the sample was naturally cooled in a vacuum environment. Then, at a fixed temperature, the nitrogen adsorption of samples under different pressures was tested. Raman spectroscopy tests were conducted on the samples using a laser Raman spectrometer (Kyoto, Japan, Horiba LabRAM HR Evolution); for the Raman test, the laser used was 532 nm, the grating was set to 2400 lines/mm, the sampling time was 45 s, and the laser power was 1 mW. The surface coating of the samples was observed using a high-resolution transmission electron microscope (MA, USA, Thermo Fisher Talos F200X G2), and the acceleration voltage was set to 3.00 kV. The crystal structure of the samples was analyzed using an X-ray diffraction (XRD) instrument (Tokyo, Japan Rigaku SmartLab SE). The elemental composition of the sample surfaces was analyzed using X-ray photoelectron spectroscopy (MA, USA, Thermo Scientific K-Alpha); the binding energy values were calibrated using the C 1 s line (284.8 eV) from the sample, with the excitation source being Al Kα radiation (hv = 1486.6 eV). The high-temperature pyrolysis process of the samples was performed using a thermogravimetric analyzer (NetzschTGA209F1).

2.5. Electrochemical test

Electrode sheets were prepared by mixing the composite material, acetylene black, and binder at a mass ratio of 8:1:1 with a targeted amount of NMP solvent to form a slurry. This slurry was then coated onto copper foils, dried, and cut into circular electrodes with a diameter of 12 mm using a coin cell punch. The mass of the active material in this composite material is 3.5 mg. The separator is composed of polypropylene, and the counter and reference electrode is made of lithium foil. Half-cells were assembled in a glove box filled with high-purity argon.

The assembled half-cells underwent cycling performance tests using a high-energy battery testing system at a current density of 0.1 $A \cdot g^{-1}$. Cyclic voltammetry (CV) and electrochemical impedance spectroscopy (EIS) measurements were conducted on the half-cells using a three-electrode system on an electrochemical workstation. The CV tests were performed within a voltage range of 0.01–3 V at a scan rate of

0.1 $mV{\cdot}s^{-1}$. The EIS tests were conducted over a frequency range of 0.01 Hz to 100 kHz with an amplitude of 5 mV. The pH value for the electrochemical measurements conducted after assembling the active material into a half-cell depends on the electrolyte used. Hence, in this work, the pH value for the electrochemical measurements was 6, indicating a weakly acidic environment.

3. Results and discussion

3.1. Structural characterization

The samples were characterized using scanning electron microscopy (SEM) observation and energy-dispersive X-ray spectroscopy (EDS). Fig. 1 presents the SEM image and EDS spectroscopic scan results of the sample NG@MoS_2. The SEM image shows layered MoS_2 particles, uniformly loaded on the surface of graphite granules. To confirm this, the EDS results indicate that the C element is clearly present within the graphite substrate, while the Mo and S elements exhibit a relatively uniform distribution across the graphite matrix. The high congruence in the distribution locations and densities of Mo and S elements substantiates that these elements are uniformly loaded onto the graphite surface in the form of MoS_2.

Fig. 2 shows the TEM images and SEM images of the sample subjected to lignin– carbon coating after MoS_2 loading, revealing a distinct lignin–carbon shell enveloping the surface of the sample. It is noteworthy that the darker portion within the red circle in Fig. 2(b) represents MoS_2 nanoparticles loaded on the surface of graphite particles. The TEM images reveal that the graphite samples are coated with a relatively uniform lignin-derived carbon layer, with a thickness ranging from a few nanometers to 30 nanometers. The composite material exhibits a quasi-spherical morphology, adorned with numerous pores on its surface, which is highly consistent with the typical graphite-like layered morphology of MoS_2 (with an interlayer spacing of approximately 0.62 nm, corresponding to the (002) peak at 14.3° in Fig. 4). In contrast, the substrate presents a flaky transparent structure, consistent with the layered crystalline morphology of NG, directly revealing the "substrate-supported particle" composite architecture. This characteristic can be attributed to two primary factors, namely, (i) the pyrolysis of lignin–carbon at elevated temperatures, and (ii) the inherent flaky structure and varying particle sizes of the graphite granules, which lead to localized inconsistencies in the microstructure post-coating.

To elucidate the internal spatial structure of the material and the pore-forming mechanism during the heat treatment process, adsorption-desorption curve analysis, specific surface area measurement, and thermogravimetric curve analysis were conducted on the samples, as illustrated in Fig. 3 and Table 1. The adsorption-desorption curve of the composite material displays a characteristic pattern indicative of typical micropore filling. Notably, the specific surface area of the NG@MoS_2@LS-C sample is 147.8267 $m^2{\cdot}g^{-1}$, confirming the formation of a porous structure arising from the pyrolysis of the lignin–carbon shell

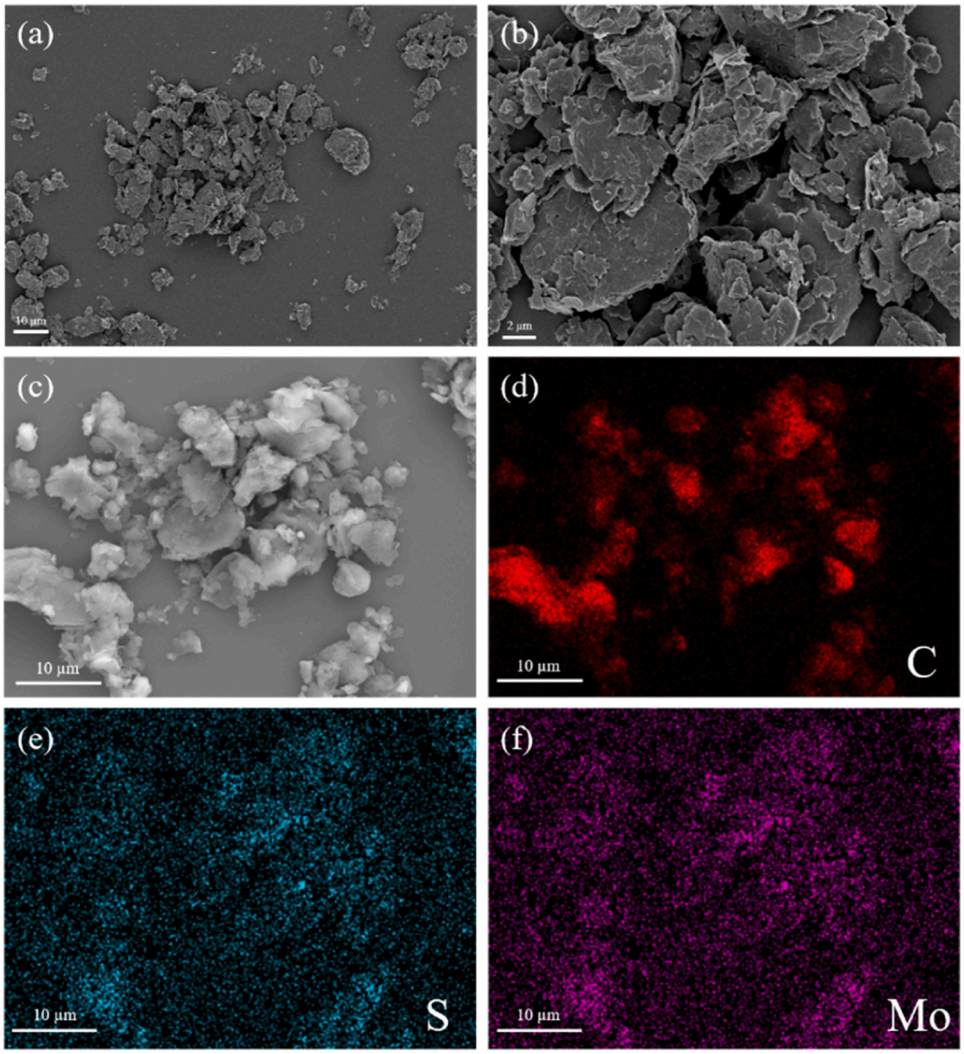

Fig. 1. SEM images (a, b) and EDS scanning images (c, d, e, f) of NG@MoS_2.

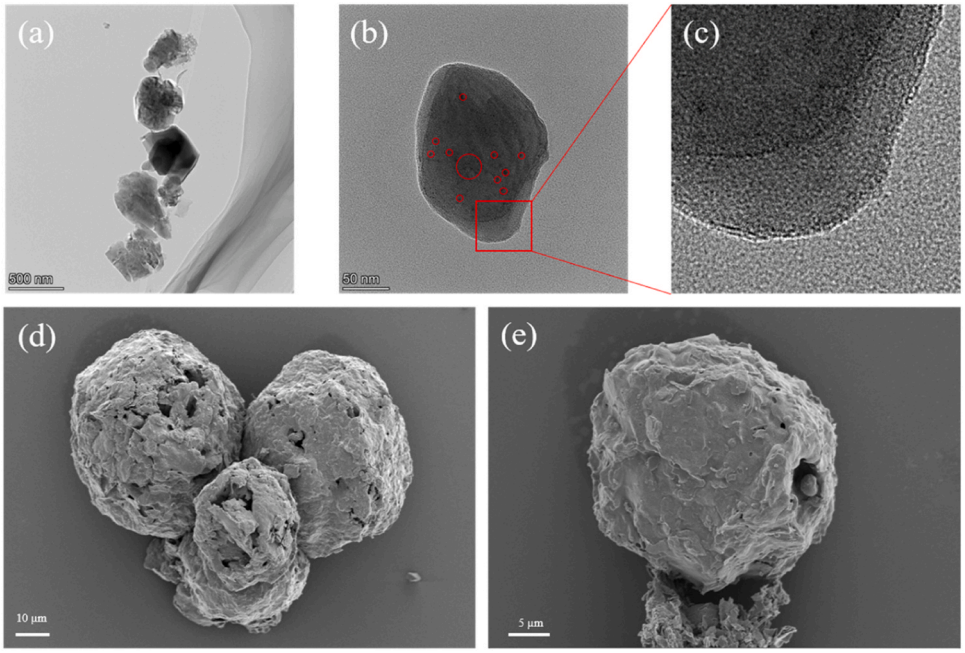

Fig. 2. TEM images (a, b and c) and SEM images (d, e) of NG@MoS_2@LS-C.

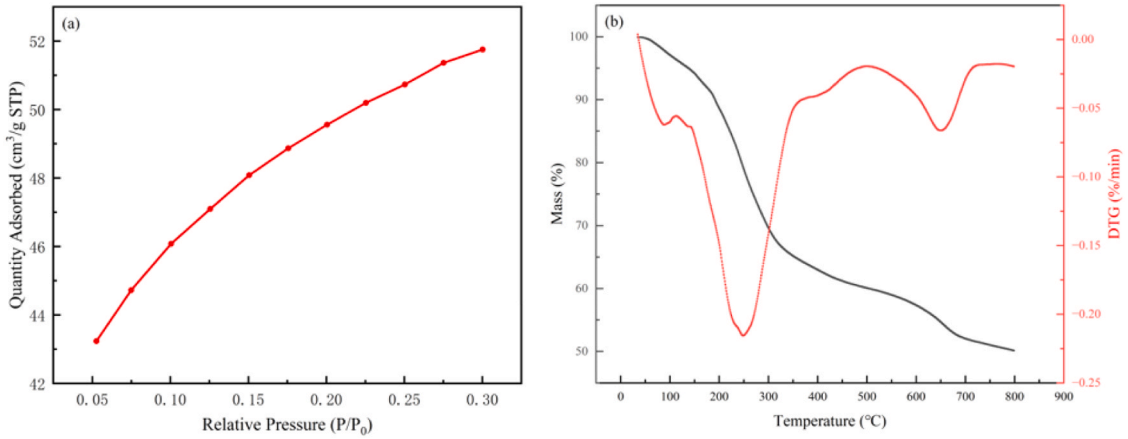

Fig. 3. N_2 adsorption and desorption curve (a) and thermogravimetric (TG)/differential thermogravimetric (DTG) curve (b) of sample NG@MoS_2@LS-C.

Table 1
Test results of specific surface area of each sample.

Sample	BET Surface Area (m^2*g^{-1})
NG	4.94
NG@MoS_2	10.91
NG@MoS_2@LS-C	147.82

during high-temperature carbonization, the mass ratio of carbon in the NG@MoS_2@LS-C composite is 73 %. This substantial specific surface area augments the reaction area, furnishing an abundance of active sites [15,16]. The pores, acting as efficient channels for ion transport, expedite the rapid migration of ions and electrons, thereby enhancing the ionic and electronic conductivity of the material. Additionally, they alleviate polarization caused by counterions, thereby conferring superior electrochemical performance [17]. Fig. 3(b) shows that the TG curve exhibits two notable inflection points, at 245 °C and 656 °C, which correspond respectively to the disappearance of functional groups linked around the benzene rings and the volatilization due to the breaking of chemical bonds surrounding the aromatic compounds within the benzene rings. At these temperatures, polymerization reactions occur among the benzene rings, leading to the formation of new polynuclear aromatic hydrocarbon compounds. As the temperature continues to rise, these compounds undergo further polycondensation to form amorphous carbon structures [18].

To reveal the phase structure of the samples, we conducted XRD analysis on them, as shown in Fig. 4. A strong and sharp peak was observed at 26°, which is attributed to the (002) peak of the graphite carbon substrate. Additionally, the reflections of the material are in high agreement with the hexagonal structure of MoS_2 (PDF#87–2416). Four intense peaks were observed at 14.3°, 32.7°, 39.3°, and 49.8°, corresponding to the (002), (100), (103), and (105) crystal planes of the MoS_2 phase, respectively [19]. The remaining crystal planes associated with graphite carbon and MoS_2 crystals are also marked individually in the figure.

To investigate the presence form of MoS_2 and the influence of the hydrothermal reaction process on the graphite substrate, Raman spectroscopy tests were conducted on the samples, with the results shown in Fig. 5. The spectrum of the sample NG@MoS_2 at the wavelength range of 350 cm^{-1} to 450 cm^{-1} is shown in Fig. 5(a). In the figure, we can observe

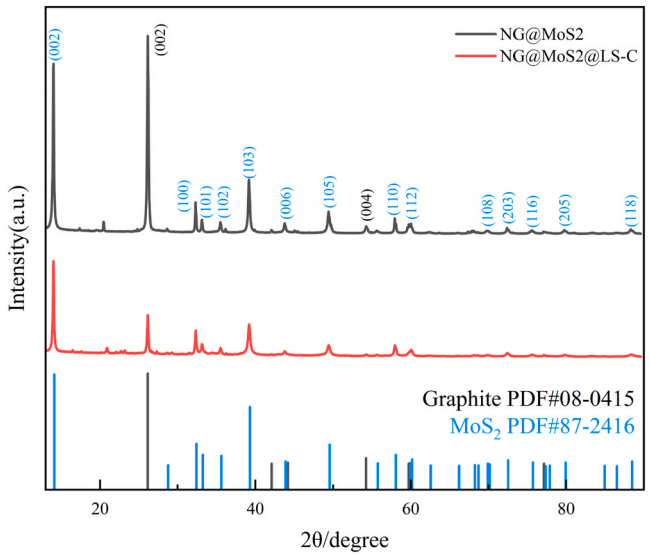

Fig. 4. XRD patterns of NG@MoS_2 and NG@MoS_2@LS-C.

two peaks, corresponding to the $E^1_{2\,g}$ vibration of MoS_2 at 380 cm^{-1} and the A_{1g} vibration at 404 cm^{-1} [20]. Compared to the peaks of monolayer MoS_2 located at 383 cm^{-1} and 402 cm^{-1}, the peaks in the figure exhibit slight red and blue shifts, respectively. This is because the different numbers of layers and aggregation states of MoS_2 manifest as variations in peak positions in the Raman spectrum. As the number of layers increases, the $E^1_{2\,g}$ and $A_{1\,g}$ vibrational peaks undergo red and blue shifts, respectively. Therefore, we can infer that MoS_2 mainly exists in the form of stacking with a small number of layers.

The figure shows two distinct D and G bands, located approximately at 1353 cm^{-1} and 1583 cm^{-1}, respectively. The emergence of the D-band is related to the breathing vibration of graphite rings that are active in the presence of disorder. When a graphite ring is excited, its internal atoms undergo breathing-like vibrations, resulting in periodic changes in the interatomic distances. This vibration mode manifests as the D-band and primarily reflects the disordered structures and defects in the sample. In contrast, the G-band arises from the stretching vibration of C═C bonds in carbon materials [21]. As shown in Fig. 5, the I_D/I_G ratio of NG@MoS_2 (0.51) is significantly higher than that of pure NG (0.33). This key Raman parameter of carbon materials intrinsically correlates with defect density and bridges structural features to electrochemical performance. The I_D/I_G ratio originates from the G peak (≈1583 cm^{-1}, indicative of ordered sp2 carbon networks) and D peak (≈1353 cm^{-1}, defect-induced). Its increase in NG@MoS_2 stems from synergistic defects: hydrothermally induced interlayer expansion causing lattice distortion, and MoS_2 growth introducing interface defects due to lattice mismatch. Electrochemically, these moderate defects enhance specific capacity by increasing active sites (for ions and charge carriers) and suppressing MoS_2 aggregation. They optimize electron/ion transport kinetics via expanded diffusion channels and intact conjugate networks. Additionally, interface defects strengthen NG@MoS_2 interactions, mitigating volume expansion and improving cycle stability. This structure-performance relationship confirms that tailoring I_D/I_G (i.e., defect density) is an effective strategy to boost the electrochemical properties of carbon-based composites for energy storage.

XPS can be used to analyze the chemical composition of the material surface. As shown in Fig. 6(a), there are many characteristic peaks present on the material surface, including O 1 s, C 1 s, Mo 3d, and S 2p. The Na element originates from both the lignin– carbon shell and the raw material used, which is sodium lignosulfonate. Among them, the high-resolution XPS results for C 1 s, S 2p, and Mo 3d of the composite material are shown in Fig. 6(b), (c) and (d), revealing the existence forms of each element in MoS_2. Fig. 6(c) presents the high-resolution XPS spectrum of S2p. From the spectrum, three pairs of peaks can be observed. The peaks at binding energies of 161.7 eV and 162.9 eV correspond to S $2p_{3/2}$ and S $2p_{1/2}$ in MoS_2, respectively, while the other two pairs of peaks correspond to R-SO_3H and Metal-S-S, respectively, originating from sodium lignosulfonate. The formation of Metal-S-S may originate from the reaction between the Mo element of MoS_2 and the doped S element in the sodium lignosulfonate shell during the high-temperature carbonization process. The XPS image of Mo 3d in Fig. 6 (d) reveals the characteristic peaks of molybdenum disulfide, specifically Mo $3d_{5/2}$ at 228.8 eV and Mo $3d_{3/2}$ at 232 eV [22]. Additionally, there are also peaks for Mo^{5+} and Mo^{6+}, which correspond to the formation of pentavalent and hexavalent molybdenum oxides due to partial oxidation of Mo during the high-temperature calcination process, such as MoO_6 [23].

We also analyzed the EDS spectrum data of samples of NG@MoS_2 and NG@MoS_2@LS-C, and the results are shown in Fig. 7. The Si and Al elements originate from the graphite ore used, while the Na element in the EDS spectrum of the sample of NG@MoS_2@LS-C is sourced from sodium lignosulfonate.

3.2. *Electrochemical characterization*

Electrode sheets were prepared by mixing the composite material, acetylene black, and binder at a mass ratio of 8:1:1 with a targeted amount of NMP solvent to form a slurry. This slurry was then coated onto copper foils, dried, and cut into circular electrodes with a diameter of 12 mm using a coin cell punch. Half-cells were assembled in a glove box filled with high-purity argon.

The assembled half-cells underwent cycling performance tests using

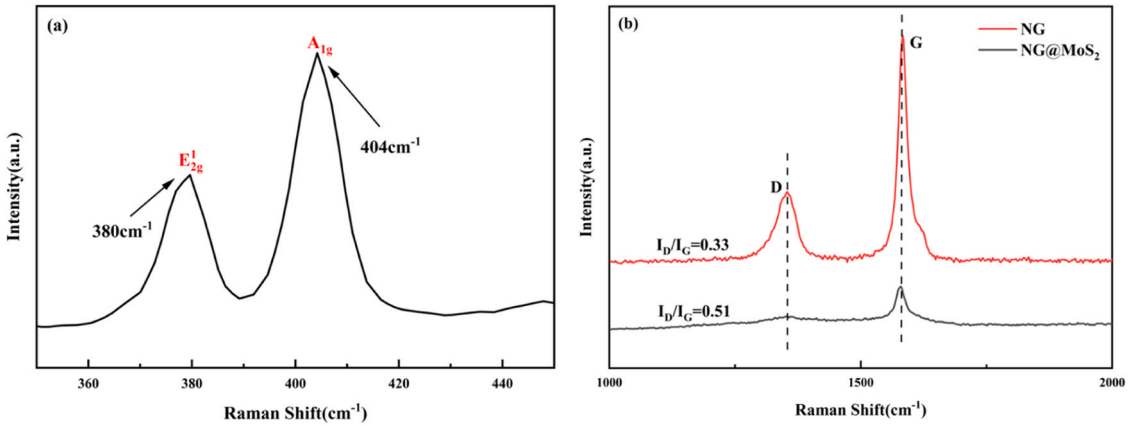

Fig. 5. Raman spectra of NG@MoS_2 of the band at 350–450 cm^{-1} (a) and Raman spectra of NG and NG@MoS_2 of the band at 1000–2000 cm^{-1} (b).

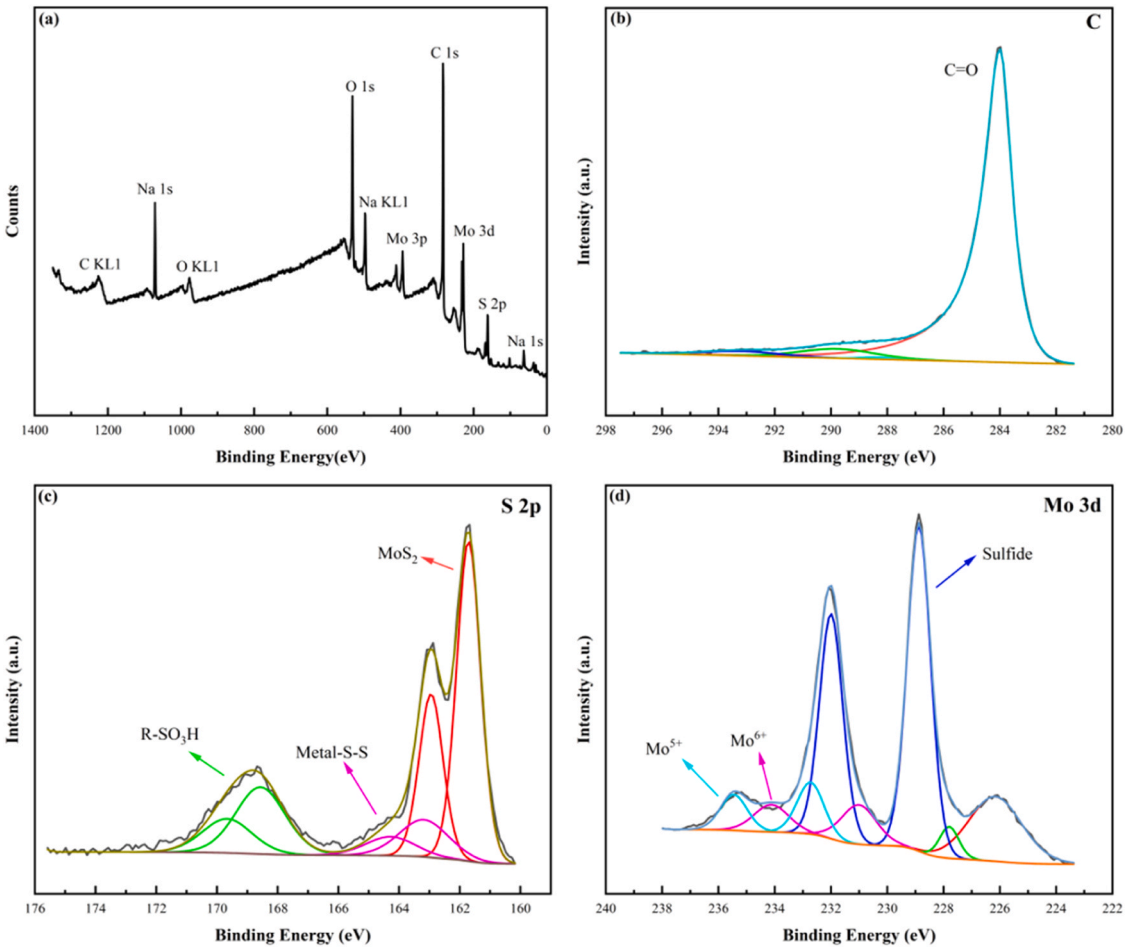

Fig. 6. XPS Spectra of NG@MoS_2@LS-C (a) and high-resolution XPS spectrum of C (b), S 2p (c), and Mo 3d (d).

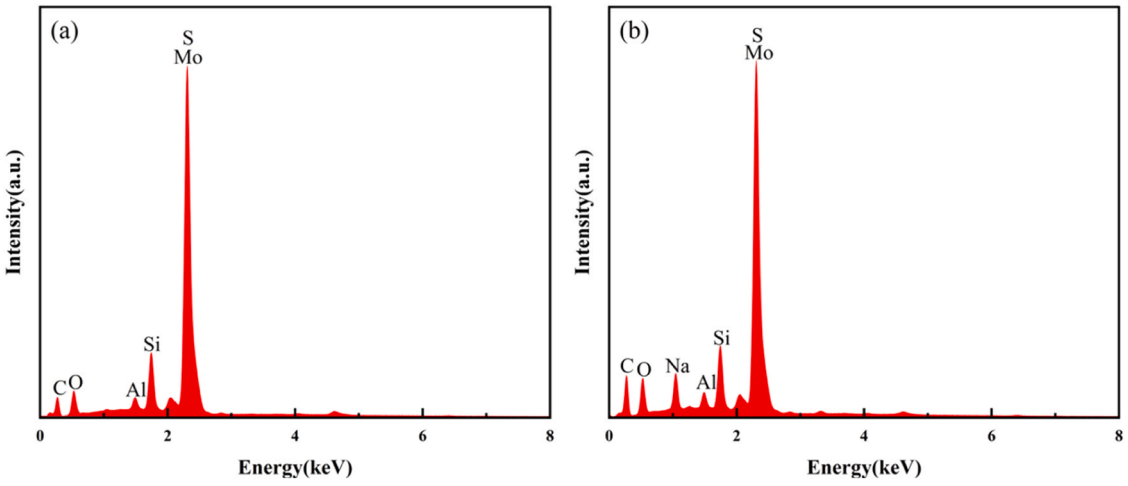

Fig. 7. EDS spectrum and the atomic percentage of individual elements of NG@MoS_2 (a) and NG@MoS_2@LS-C (b).

a high-energy battery testing system at a current density of 0.1 $A{\cdot}g^{-1}$. Cyclic voltammetry (CV) and electrochemical impedance spectroscopy (EIS) measurements were conducted on the half-cells using a three-electrode system on an electrochemical workstation. The CV tests were performed within a voltage range of 0.01–3 V at a scan rate of 0.1 $mV{\cdot}s^{-1}$. The EIS tests were conducted over a frequency range of 0.01 Hz to 100 kHz with an amplitude of 5 mV. The pH value for the electrochemical measurements conducted after assembling the active material into a half-cell depends on the electrolyte used. Hence, in this study, the pH value for the electrochemical measurements is 6, indicating a weakly acidic environment.

After assembling the battery into a coin-cell configuration, its cycling performance was evaluated using a high-performance battery testing system. The cyclic test was conducted at a current density of 100 $mA{\cdot}g^{-1}$ within a voltage range of 0.01–3 V. The cycle test results are shown in Fig. 8. Notably, the sample exhibits a high initial capacity of

588.2 mAh·g^{-1} , which remains robust through retaining a reversible capacity of 326.2 mAh·g^{-1} , even after 30 cycles, demonstrating both high specific capacity and excellent cycling stability. This exceptional performance can be attributed to the lignin-derived porous carbon shell, which provides efficient electronic pathways from the current collector to the graphite and MoS_2 particles, facilitating the synergistic transport of electrons and lithium ions [24]. Furthermore, the carbon shell acts as a protective barrier, minimizing direct contact between the active material and the electrolyte, thereby preventing the formation of unstable solid–electrolyte interphase (SEI) films and mitigating volume expansion during Li^+ insertion into the electrode material. The lignin-derived carbon coating layer, featuring a porous architecture and robust mechanical strength, serves as a key structural modifier to accommodate the volume variation of MoS_2 during charge-discharge cycles. Specifically, the interconnected porous structure provides sufficient buffer space to relieve the internal stress induced by the volumetric expansion (over 100 %) of MoS_2 (especially during the conversion reaction), while its inherent mechanical rigidity forms a flexible yet durable support network. This dual effect not only suppresses the aggregation and peeling of MoS_2 nanoparticles but also maintains the integrity of the electrode structure and the continuity of electron/ion transport pathways, thereby synergistically enhancing the cycling stability of the composite. This stabilization of the material structure contributes significantly to enhancing its specific capacity and cycling stability [25]. Furthermore, Figs. 8a and 8(b) present the cycling performance of NG and NG@LS-C from different groups at the same current density as controls.

In order to analyze the electrochemical reaction mechanism and lithium storage mechanism of the materials, we tested the samples using cyclic voltammetry. Fig. 9 shows the CV curves of NG@MoS_2@LS-C, indicating a wide reduction peak at about 1.5 V, which corresponds to the formation of the Li$_x$$MoS_2$ interlayer compound when Li^+ is inserted into the MoS_2 lattice, accompanied by the reduction reaction of MoS_2 (i.e., conversion to Li_2S and Mo). A sharp oxidation peak is observed around 1.9 V, attributed to the complete reaction between Li^+ and MoS_2. Relative to the lithium removal of the unconverted residual Li$_x$$MoS_2$ interlayer compound, the lithium removal oxidation reaction of MoS_2 is more dominant [26]. In NG@MoS_2@LS-C composites, lithium storage mechanisms evolve: conversion reaction (MoS_2→Mo+Li_2S) dominates initial cycles, contributing high capacity but causing irreversible decay via SEI formation, Li_2S dissolution, and volume expansion. Subsequent cycles see intercalation (Li^+→Li$_x$$MoS_2$) become dominant, enabled by NG/LS-C's conductivity and structural support,

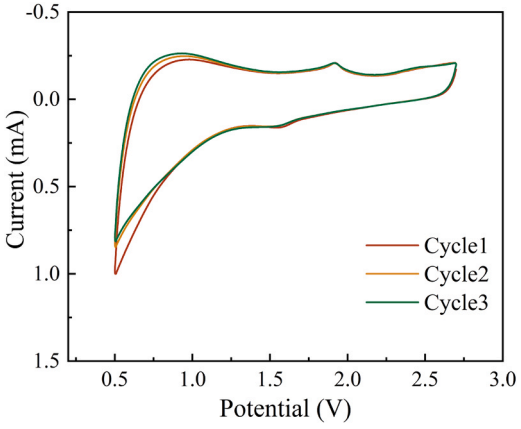

Fig. 9. Cyclic voltammetry test results of sample NG@MoS_2@LS-C.

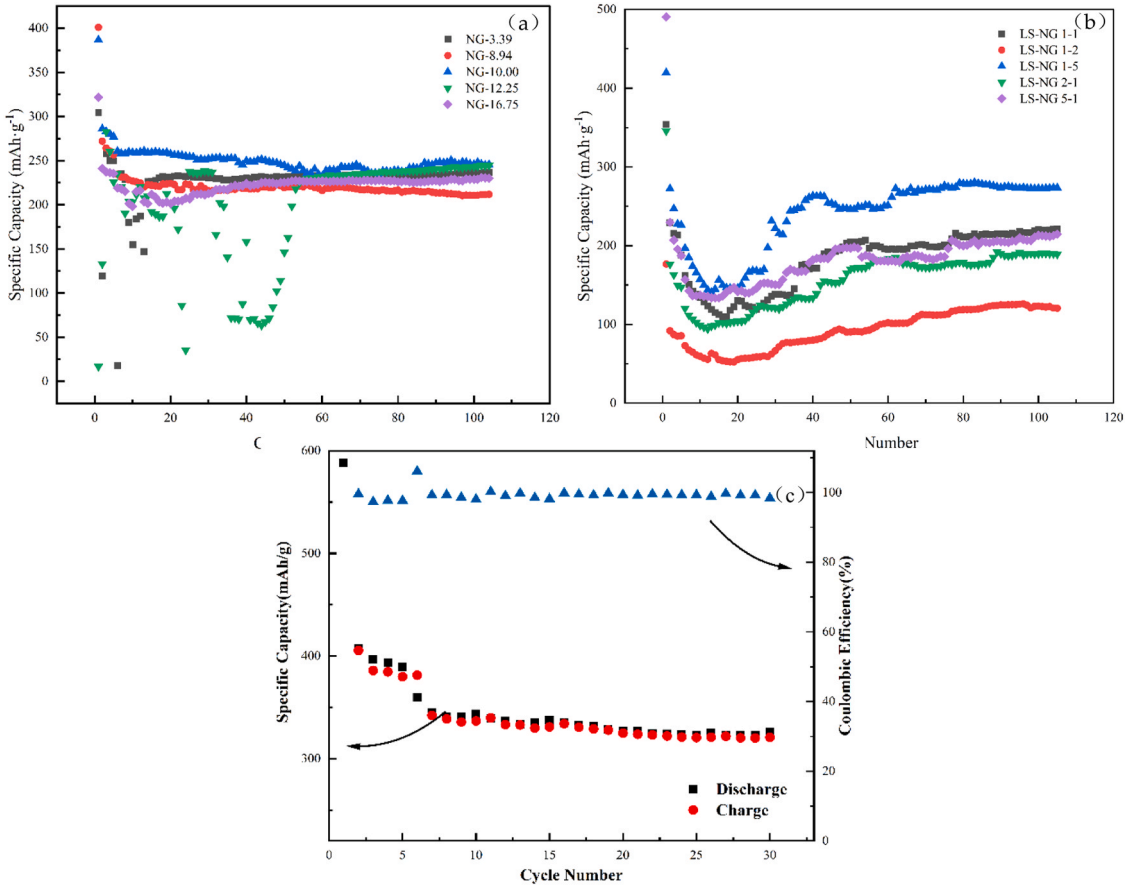

Fig. 8. Cyclic performance of NG samples (a), Cyclic performance of each group of NG@LS-C samples(b), Cyclic test results of NG@MoS2@LS-C sample (c).

which stabilize the electrode and enhance cycling stability. This evolution stems from structural stabilization and kinetic optimization, linking the dominant mechanism to capacity retention [27].

The specific lithiation reaction process is displayed as follows:

$$MoS_2 + xLi^+ + xe^- \rightarrow Li_xMoS_2$$

$$MoS_2 + 4Li^+ + 4e^- \rightarrow Mo + 2Li_2S$$

$$Li_xMoS_2 + (4-x)Li^+ + (4-x)e^- \rightarrow Mo + 2Li_2S$$

$$C_6 + xLi^+ + xe^- \rightarrow Li_xC_6$$

The EIS spectra and fitting curves of various samples within the frequency range of 0.01–100,000 Hz are presented in Fig. 10. All the curves consist of a semicircle in the high-frequency region and a sloping line in the low-frequency region. In the high-frequency range, a larger diameter of the semicircle indicates a higher charge transfer resistance (R_{ct}) of the electrode material. The results of the electrochemical impedance fitting are summarized in Table 2, where R_s represents the electrolyte resistance and R_{ct} denotes the charge transfer resistance, both in the high-frequency region. Notably, we observe that the R_{ct} value of NG reaches a high value of 411.6 Ω, whereas that of NG@MoS_2@LS-C is significantly reduced to only 158 Ω. Since R_{ct} reflects the ease of the electrochemical reaction, with a smaller R_{ct} implying superior electron/ion transport capabilities, the results indicate that the loading of MoS_2 and the coating effect of lignin-derived carbon significantly diminish the lithium-ion transfer resistance at the electrode material interface. By means of electrochemical impedance spectroscopy (EIS) and diffusion coefficient data, we can gain insights into a) The carbon layer, with its high conductivity, constructs continuous electronic conduction pathways to accelerate electron transfer, as evidenced by reduced charge transfer resistance (Rct) in EIS Nyquist plots; b) MoS_2's layered structure provides abundant interlayer channels, facilitating Li^+ intercalation/deintercalation and diffusion, reflected in higher diffusion coefficients compared to non-layered analogs; c) Collectively, they form an electron-ion dual-transport network: the carbon layer addresses MoS_2's poor conductivity, while MoS_2 compensates for the carbon shell's limited ion diffusion sites. This synergy significantly lowers Rct and enhances Li^+ diffusion rate, thereby improving overall electrochemical performance.

Table 2
EIS results of all samples.

Sample	R_s (Ω)	R_{ct} (Ω)	D_{Li}^+($cm^2 \cdot s^{-1}$)
NG	6.23	403.0	3.26×10^{-14}
NG@MoS_2	4.34	209.4	8.29×10^{-14}
NG@MoS_2@LS-C	5.76	168.2	2.02×10^{-13}

In the low-frequency region, the EIS curve approximates a straight line, with its slope correlated to the lithium-ion diffusion coefficient (D_{Li}^+) within the electrode material. The following formula can be utilized to calculate D_{Li}^+ based on the data from the low-frequency region, providing a qualitative analysis of the ion diffusion coefficient for the composite material:

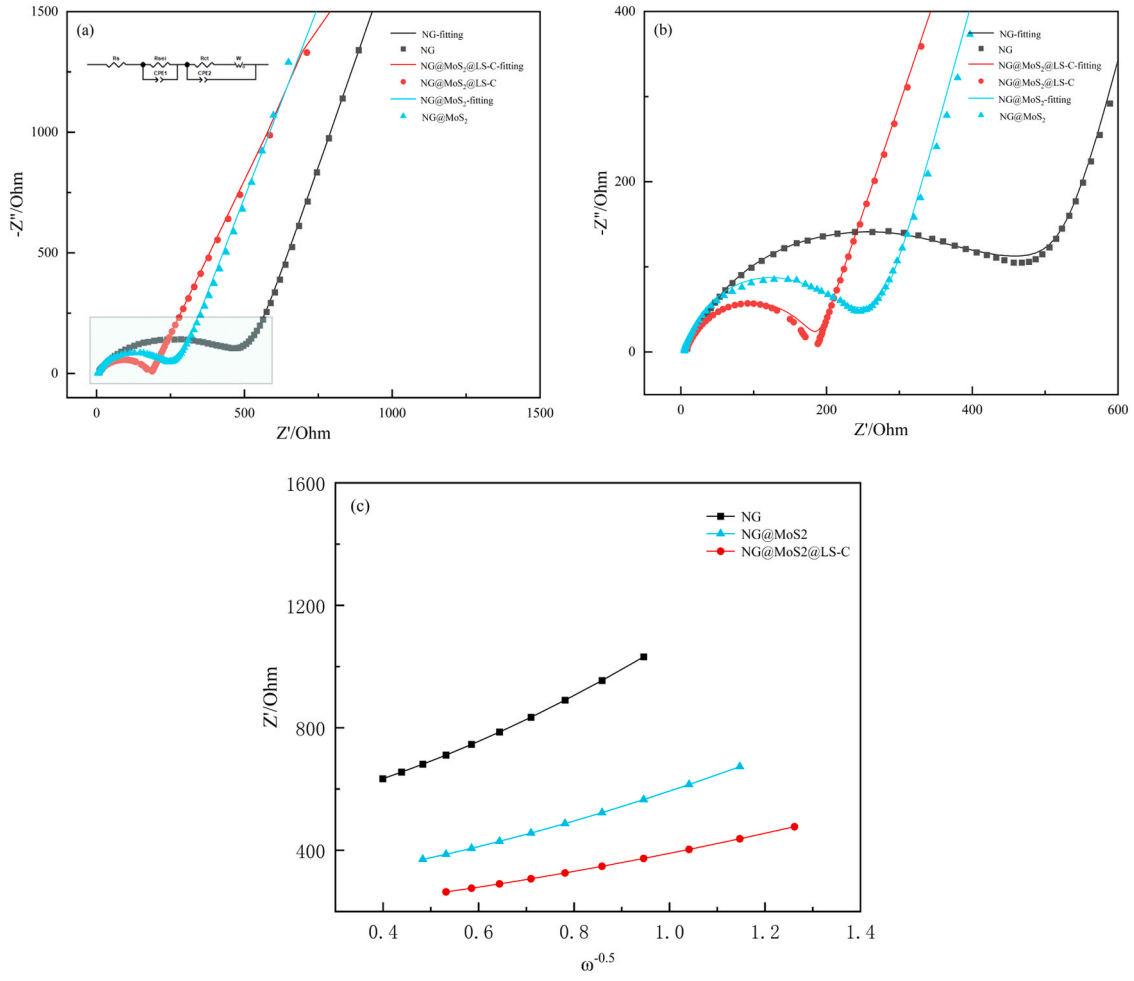

Fig. 10. EIS spectrogram of each sample (a), enlarged diagram of high-frequency region (b) and fitting relation diagram of Z' and $\omega^{-0.5}$ in low-frequency region (c).

$$D_{Li^+} = \frac{R^2T^2}{2A^2n^4F^4C_{Li^+}{}^2\sigma_\omega{}^2} \quad (1\text{-}1)$$

$$Z' = R_S + R_{ct} + \sigma_\omega \bullet \omega^{-0.5} \quad (1\text{-}2)$$

where R represents the gas constant (8.314 J/K·mol); T is the absolute temperature at which the impedance test is conducted (set at 298 K); A is the surface area of the electrode disk (with a diameter of 12 mm); n is the number of electrons transferred per molecule during the oxidation reaction at the electrode; F is the Faraday constant (96,500 C/mol); C_{Li}^+ denotes the concentration of lithium ions in the electrode material; and σ_ω is the Warburg impedance factor. By selecting sample points from the low-frequency region and fitting Z' against $\omega^{-0.5}$, the fitted slope σ_ω can be obtained. Substituting σ_ω into Equation 1–1, the diffusion coefficient D_{Li}^+ of Li^+ can be determined.

To further investigate the ionic diffusion properties of the materials, Z′ was plotted against $\omega^{-0.5}$, with the results in Fig. 10(d) demonstrating a good fit. The calculated D_{Li}^+ values are reported in Table 2. The D_{Li}^+ value of the NG@MoS_2@LS-C sample is 2.02×10^{-13}, which is higher than that of NG@MoS_2 (i.e., without the lignin–carbon coating) and an order of magnitude greater than that of pristine natural graphite. This enhancement is attributed to the presence of the lamellar structure within the molybdenum disulfide layers, which facilitates better contact between the active MoS_2 material and the electrolyte structure during charge-discharge processes, effectively reducing resistance and enhancing electrochemical kinetics [28]. Furthermore, the external lignin–carbon coating mitigates side reactions between the active material surface and the electrolyte, acting as a "buffer layer" for lithium-ion transport. The preferential adsorption and storage of lithium ions by the carbon layer facilitate their smooth intercalation, reducing local concentration gradients and stress concentrations, thus promoting the synergistic transport of electrons and ions [29].

Table 3 provides a summary of the electrochemical performance from published high-performance data for comparative analysis. The synthesized NG@MoS_2@LS-C demonstrated a high initial capacity of 588.2 mAh·g^{-1} and maintained a capacity of 326.2 mAh·g^{-1} after 30 cycles, indicating superior lithium storage performance in comparison to previous literature reports.

4. Conclusions

This study focuses on the development of high-performance anode materials for lithium-ion batteries (LIBs) to meet the growing demands for high energy density, excellent cycle stability, and low cost. Addressing the limitations of conventional graphite anodes, such as low specific capacity and poor rate charge-discharge capability, an innovative modification method is proposed. This method involves uniformly depositing MoS_2 nanoparticles on the surface of natural graphite (NG) via hydrothermal synthesis, followed by coating and carbonization with sodium lignosulfonate (LS), resulting in the NG@MoS_2@LS-C composite material. NG serves as a crucial capacity contributor in the composite, rendering a notable contribution to the total capacity of LIBs. For the contribution mechanism, NG stores lithium via the classic lithium-ion intercalation/deintercalation pathway—specifically, Li^+ intercalates between graphite layers to form LiC_6 alloy (reaction formula: $C_6 + xLi^+ + xe^- \rightarrow Li_xC_6$)—with a theoretical specific capacity of 372 mAh·g^{-1}. Regarding the verification of practical contribution, the lithium-ion diffusion coefficient (3.26×10^{-14} $cm^2 \cdot s^{-1}$) and charge transfer resistance (403.0 Ω) of NG reported in the study confirm its electrochemical activity. Within the NG@MoS_2@LS-C composite, NG not only provides the fundamental capacity but also acts as a conductive framework to facilitate electron/ion transport, thereby enhancing the overall capacity performance.

Experimental results demonstrate that the incorporation of MoS_2 nanoparticles significantly enhances the cycling performance of the composite. The initial Coulombic efficiency loss induced by the defects in the lignin-derived carbon shell can be compensated for by its enhanced cycling stability and capacity retention, thereby being conducive to the practical application of the material. Moreover, the lamellar structure of the MoS_2 nanoparticles, combined with the buffering and electrolyte-blocking effects of the lignin-derived carbon shell, endow the composite with exceptional electron-ion synergetic transport properties. Results indicate that the composite exhibits an initial capacity of 588.2 mAh·g^{-1} at a current density of 100 mA·g^{-1} and retains a reversible capacity of 326.2 mAh·g^{-1} after 30 cycles, showcasing its outstanding electrochemical performance.

Furthermore, when analyzing the causes of capacity fading, several aspects need to be considered, namely irreversible conversion reactions, detachment of active materials, continuous growth of the solid electrolyte interphase (SEI) film, or agglomeration of MoS_2. These are among the primary factors contributing to capacity fading. However, based on relevant literature, the dominant cause should be the agglomeration of MoS_2. The capacity fading of MoS_2-based materials is the result of the synergistic effect of multiple factors, including structural damage, volume effect, SEI film instability, and failure of the transport network.

In summary, this study successfully fabricates an NG@MoS_2@LS-C anode material for LIBs with high specific capacity and exceptional cycle stability, presenting broad application prospects in the field of LIB anode materials. This material not only overcomes the shortcomings of traditional graphite anodes, but also provides a new avenue for achieving green and sustainable development. Future research will aim to further optimize the material preparation process and explore its application in practical battery systems, thereby driving the advancement of LIB technology.

Table 3
Summary of published reports of electrochemical performance of graphite-based anodes, compared to the current study.

Materials	Initial specific capacity (Current density)	Reversible specific capacity (Cycles)	References
Carbon coated Cu_6Sn_5/graphite composite anodes	303 mAh·g^{-1} (0.1 C)	200 mAh·g^{-1} (20)	[30]
P/EG	389 mAh·g^{-1} (0.1 C)	/	[31]
G-CuO	347 mAh·g^{-1} (0.1 mA·cm^{-2})	/	[32]
MoS_2/graphite composite	358.2 mAh·g^{-1} (100 mA·g^{-1})	244 mAh·g^{-1} (800)	[33]
Graphite/Si@TiO_2	675 mAh·g^{-1} (500 mA·g^{-1})	506 mAh·g^{-1} (100)	[34]
NG	395 mAh·g^{-1} (100 mA·g^{-1})	367 mAh·g^{-1} (100)	[35]
NG@MoS_2	506 mAh·g^{-1} (50 mAh·g^{-1})	405.25 mAh·g^{-1} (100)	[36]
NG@MoS_2@LS-C	588.2 mAh·g^{-1} (100 mA·g^{-1})	326.2 mAh·g^{-1} (30)	This study

CRediT authorship contribution statement

Wenyu Wang: Validation. **Yifei Chen:** Validation. **Huhao Kong:** Formal analysis. **Yuqi Liu:** Investigation. **Xiaoping Jiang:** Resources. **Yongchao Yao:** Data curation. **He Chen:** Data curation. **Jia Wei Chew:** Writing – review & editing. **Jiazhe Sun:** Writing – review & editing, Writing – original draft, Visualization, Methodology, Formal analysis, Conceptualization. **Zhengping Zhao:** Supervision, Software, Resources, Project administration, Methodology, Investigation, Funding acquisition, Data curation, Conceptualization. **Zhao Xu:** Validation, Formal analysis. **Shuqi Sheng:** Investigation. **Shengyi Zhao:** Visualization.

Funding

This research was supported by the Shandong Provincial Science and

Technology Innovation Capability Improvement Project for Small and Medium-sized Enterprises (SMEs) [Grant No. 2025TSGCCZZB0952], which specifically funded the synthesis, characterization, and lithium-ion battery anode performance evaluation of MoS_2-based composite materials in this work.

Declaration of Competing Interest

The authors declare that they have no known competing financial interests or personal relationships that could have appeared to influence the work reported in this paper.

Data Availability

The authors can confirm that all relevant data are included in the article.

References

[1] X. Yin, W. Chen, J. Eom, E. Leon, Clarke, H. Son, L. Kim, G. Pralit, Patel, Page Kyle, China's transportation energy consumption and CO_2 emissions from a global perspective, Energy Policy 82 (2015) 233–248, https://doi.org/10.1016/j.enpol.2015.03.021.

[2] H. Wang, X. Yang, Q. Wu, Q. Zhang, H. Chen, H. Jing, C. Niu, Encapsulating silica/antimony into porous electrospun carbon nanofibers with robust structure stability for high-efficiency lithium storage, ACS nano 12 (2015) 3406–3416, https://doi.org/10.1021/acsnano.7b09092.

[3] H. Zhang, Y. Yang, D. Ren, L. Wang, X. He, Graphite as anode materials: fundamental mechanism, recent progress and advances, Energy Storage Mater. 36 (2021) 147–170, https://doi.org/10.1016/J.ENSM.2020.12.027.

[4] W. Zhao, C. Zhao, H. Wu, L. Li, C. Zhang, Progress, challenge and perspective of graphite-based anode materials for lithium batteries: a review, J. Energy Storage 81 (2024) 110409, https://doi.org/10.1016/j.est.2023.110409.

[5] H.S.S. RamakrishnaMatte, A. Gomathi, A.K. Manna, D.J. Late, R. Datta, S.K. Pati, C. N.R. Rao, MoS_2 and WS_2 analogues of graphene, Angew. Chem. Int. Ed. 49 (2010) 4059–4062, https://doi.org/10.1002/anie.201000009.

[6] K. Bindumadhavan, S.K. Srivastava, S. Mahanty, MoS_2–MWCNT hybrids as a superior anode in lithium-ion batteries, Chem. Commun. 49 (2013) 1823–1825, https://doi.org/10.1039/C3CC38598A.

[7] X. Cao, Y. Shi, W. Shi, X. Rui, Q. Yan, J. Kong, H. Zhang, Preparation of MoS_2-coated three-dimensional graphene networks for high-performance anode material in lithium-ion batteries, Small 9 (2013) 3433–3438, https://doi.org/10.1002/smll.201202697.

[8] K. Chang, W. Chen, l-cysteine-assisted synthesis of layered MoS_2/graphene composites with excellent electrochemical performances for lithium ion batteries, ACS Nano 5 (2011) 4720–4728, https://doi.org/10.1021/nn200659w.

[9] T. Saito, R.H. Brown, M.A. Hunt, D.L. Pickel, J.M. Pickel, J.M. Messman, F.S. Baker, M. Keller, A.K. Naskar, Turning renewable resources into value-added polymer: development of lignin-based thermoplastic, Green. Chem. 14 (2012) 3295–3303, https://doi.org/10.1039/C2GC35933B.

[10] X.-P. Ouyang, Y. Yang, G.-D. Zhu, X.-Q. Qiu, Radical synthesis of tetrameric lignin model compound, Chin. Chem. Lett. 26 (2015) 980–982, https://doi.org/10.1016/j.cclet.2015.05.011.

[11] X. Wang, Q. Zhang, C. Nam, M. Hickner, M. Mahoney, M.E. Meyerhoff, An ionophore-based anion-selective optode printed on cellulose paper, Angew. Chem. Int. Ed. 56 (2017) 11826–11830, https://doi.org/10.1002/anie.201706147.

[12] W.-J. Chen, C.X. Zhao, B.Q. Li, T.Q. Yuan, Q. Zhang, Lignin-derived materials and their applications in rechargeable batteries, Green. Chem. 24 (2022) 565–584, https://doi.org/10.1039/D1GC02872C.

[13] H. Yue, S. Chen, S. Zhang, X. Yan, W. Li, T. Li, Y. Gao, Preparation and electrochemical properties of flexible self-supported graphene/silicon/carbon nanotube composite electrode for lithium-ion battery, J. Alloy. Compd. 1004 (2024) 175858, https://doi.org/10.1016/J.JALLCOM.2024.175858.

[14] Y. Sheng, Y. Wang, S. Yin, Niobium-based oxide for anode materials for lithium-ion batteries, Chemistry 30 (2023) e202302865, https://doi.org/10.1002/CHEM.202302865.

[15] J. Liang, S. Chen, M. Xie, Y. Wang, X. Guo, X. Guo, W. Ding, Expeditious fabrication of flower-like hierarchical mesoporous carbon superstructures as supercapacitor electrode materials, Mater. Chem. A 2 (2014) 16884–16891, https://doi.org/10.1039/C4TA03209H.

[16] H. Fan, X. Hu, S. Zhang, Z. Xu, G. Gao, Y. Zheng, G. Hu, Q. Chen, T.S. AlGarni, R. Luque, Flower-like carbon cathode prepared via in situ assembly for Zn-ion hybrid supercapacitors, Carbon 180 (2021) 254–264, https://doi.org/10.1016/j.carbon.2021.04.093.

[17] Z. Zhao, Z. Xu, Z. Zheng, W. Wang, W. Wang, X. Yang, J.W. Chew, Preparation and lithium storage performance of SiO_2/Ag composite materials coated with polyphosphazene, Express Polym. Lett. 18 (2024) 976–990, https://doi.org/10.3144/expresspolymlett.2024.75.

[18] F. Chen, L. Wu, Z. Zhou, J. Ju, Z. Zhao, M. Zhong, T. Kuang, MoS_2 decorated lignin-derived hierarchical mesoporous carbon hybrid nanospheres with exceptional Li-ion battery cycle stability, Chin. Chem. Lett. 30 (2019) 197–202, https://doi.org/10.1016/j.cclet.2018.10.007.

[19] S.H. Cho, J.H. Kim, I.G. Kim, J.H. Park, J.W. Jung, H.S. Kim, I.D. Kim, Reduced graphene-oxide-encapsulated MoS_2/carbon nanofiber composite electrode for high-performance Na-ion batteries, Nanomaterials 11 (2021) 2691, https://doi.org/10.3390/nano11102691.

[20] M.D. Maratos, A. Michail, A. Stamatelatos, Enhanced Raman scattering in CVD-grown MoS_2/Ag nanoparticle hybrids, Materials 17 (2024) 4396, https://doi.org/10.3390/MA17174396.

[21] O.A. Streletskiy, I.A. Zavidovskiy, I.F. Nuriahmetov, O.Y. Nishchak, A.V. Pavlikov, N.F. Savchenko, Resistive gas sensors based on porous Sp-containing films obtained by dehydrohalogenation of PVDC and PVDC-PVC copolymer, C. J. Carbon Res. 9 (2023) 82, https://doi.org/10.3390/c9030082.

[22] Z. Junpu, X. Wen, Y. Feng, Constructing MoS_2-SnS heterostructures on N-doped carbon nanosheets for enhanced catalytic conversion of polysulfides in lithium-sulfur batteries, Chem. Eng. J. 475 (2023), https://doi.org/10.1016/J.CEJ.2023.146009.

[23] I. Roman, Romanov, V. Ivan, Zabrosaev, A. Anastasia, Chouprik, S. Sergey, Zarubin, I. Dmitry, A. Yakubovsky, Ilya, Zavidovskiy, Andrey M. Markeev, Impact of water vapor on the 2D MoS_2 growth in metal-organic chemical vapor deposition, Vacuum 230 (2024) 113739, https://doi.org/10.1016/J.VACUUM.2024.113739.

[24] V. Nulu, A. Nulu, K.Y. Sohn, Hierarchical hollow porous structures of nickel-doped λ-MnO_2 anodes for Li-ion energy storage systems, Nanoscale Adv. 6 (2024) 3426–3440, https://doi.org/10.1039/D4NA00023D.

[25] K. Wang, H. Li, X. Chen, Z. Wan, T. Wu, W. Ahmad, D. Qian, X. Wang, J. Gao, R. Khan, Bi-directional H-bonding modulated soft/hard polyethylene glycol-polyaniline coated si-anode for high-performance Li-Ion Batteries, Small Methods (2024) 2301667, https://doi.org/10.1002/smtd.202301667.

[26] Z. Zhou, F. Chen, Z. Jiang, T. Liu, Y. Fei, T. Kuang, M. Zhong, X. Liu, S. Song, MoS_2 nanosheets uniformly grown on polyphosphazene-derived carbon nanospheres for lithium-ion batteries, Surf. Interfaces 24 (2021) 101034, https://doi.org/10.1016/j.surfin.2021.101034.

[27] L. Wang, H. Yan, L. Chen, X. Ji, Y. Lin, B. Wang, C. Hao, Preparation of a MIL-125/MoS_2/SiO_2 ternary nanohybrid and its smart electrorheological behavior, ACS Appl. Mater. Interfaces 16 (2024) 59302–59314, https://doi.org/10.1021/ACSAMI.4C12828.

[28] Z. Zhou, F. Chen, L. Wu, T. Kuang, X. Liu, J. Yang, P. Fan, Z. Fei, Z. Zhao, M. Zhong, Heteroatoms-doped 3D carbon nanosphere cages embedded with MoS_2 for lithium-ion battery, Electro Acta 332 (2020) 135490, https://doi.org/10.1016/j.electacta.2019.135490.

[29] Y. Liu, P. Wang, Z. Yang, L. Wang, Z. Li, C. Liu, B. Liu, Z. Sun, H. Pei, Z. Lv, Lignin derived ultrathin all-solid polymer electrolytes with 3D single-ion nanofiber ionic bridge framework for high performance lithium batteries, Adv. Mater. 36 (2024) 2400970, https://doi.org/10.1002/adma.2024.00970.

[30] N. Jayaprakash, N. Kalaiselvi, C.H. Doh, Synthesis and electrochemical evaluation of carbon coated Cu_6Sn_5 alloy-graphite composite lithium battery anodes, Appl. Electrochem 37 (2007) 567–573, https://doi.org/10.1007/s10800-006-9286-9.

[31] H. Zheng, D.Y. Park, M.S. Kim, Preparation and characterization of anode materials using expanded graphite/pitch composite for high-power Li-ion secondary batteries, Res. Chem. Inter. 40 (2014) 2501–2507, https://doi.org/10.1007/s11164-014-1660-3.

[32] H. Huang, E.M. Kelder, J. Schoonman, Graphite–metal oxide composites as anode for Li-ion batteries, Power Sources 97-98 (2001) 114–117, https://doi.org/10.1016/S0378-7753(01)00597-3.

[33] Q. Yang, M. Liu, Y. Hu, Y. Xu, L. Kong, L. Kang, Facile synthesis of MoS_2/graphite intercalated composite with enhanced electrochemical performance for sodium ion battery, Energy Chem. 27 (2018) 1208–1213, https://doi.org/10.1016/j.jechem.2017.08.009.

[34] B.N. Vats, R. Gupta, A. Gupta, S. Fatima, D. Kumar, Enhancing Li-ion battery performance through the integration of Si@TiO_2 core-shell nanoparticles with natural graphite, Chem. Sel. 9 (2024) e202303545, https://doi.org/10.1002/slct.2023.03545.

[35] A. Wang, F. Liu, Z. Wang, X. Liu, Self-assembly of silicon/carbon hybrids and natural graphite as anode materials for lithium-ion batteries, RSC Adv. 6 (2016) 104995–105002, https://doi.org/10.1039/C6RA20131H.

[36] J. Li, F. Hu, H. Wei, J. Hei, Y. Yin, G. Liu, H. Wei, Confining MoS_2/C nanoparticles on two-dimensional graphene sheets for high reversible capacity and long-life potassium ions batteries, Compos. Part B 250 (2023), https://doi.org/10.1016/J.COMPOSITESB.2022.110424.